A topological classification for intersection singularities of exceptional surfaces in pseudo-Hermitian systems

Hongwei Jia[#], Ruo-Yang Zhang[#], Jing Hu, Yixin Xiao, Yifei Zhu[*], C. T. Chan[†]

Abstract: Exceptional degeneracy plays a pivotal role in the topology of non-Hermitian systems, and recently many efforts have been devoted to classifying exceptional points and exploring the intriguing physics. However, intersections of exceptional surfaces, which are commonly present in non-Hermitian systems with parity-time symmetry or chiral symmetry, were not classified. Here we classify generic pseudo-Hermitian systems, for which the momentum space is partitioned by exceptional surfaces, and these surfaces intersect stably therein. The topology of such gapless structure can be viewed from its quotient space, which is "figure eight," by considering the equivalence relations of eigenstates in energy gaps and on exceptional surfaces. We reveal that the topology of such systems can be described by a free non-Abelian group composed of products of two generators. The topological invariants in the group are well associated with the spin rotation of eigenstates via adiabatic transformations. Our classification does not rely on specific bandgaps and is thus a global topological description. Importantly, the classification predicts a new phase of matter, and can systematically explain how the exceptional surfaces and their intersections evolve against deformations to the Hamiltonian. Our work opens a new pathway for designing systems with robust topological phases, and is potentially a guidance for applications to sensing and lasing devices utilizing exceptional surfaces and intersections.

Introduction: Singularities, characterized by the property of non-differentiability, constitute an important part in the real world. The occurrence of a singularity is always accompanied with exotic physical phenomena [1,2,3,4,5,6,7,8,9,10,11,12,13]. As a prime example, a Weyl point in Hermitian systems act as a drain or source of the Berry curvature, and the Fermi-arc surface state links two Weyl points with opposite chiralities [1,2,9,11]. A pivotal way for understanding singularities is the topology. A singularity is characterized by a topological invariant (e.g. Chern number), which can be calculated with the adiabatic evolution of eigenstates on loops/surfaces enclosing the singularity [5,6,7,8,9,11]. Recently, the topology of non-Hermitian systems is attracting growing attention [14,15,16,17,18,19,20,21,22,23,24]. Non-Hermiticity is ubiquitous because most systems are not isolated. The eigenenergies become complex, representing energy exchange with surrounding environment. Exceptional point, defined on complex energy plane, is thus a unique feature of non-Hermiticity, and is a singular point that both of the eigenenergies and eigenstates coalesce [14,15,16,18,19]. Different from Weyl points and nodal lines in Hermitian systems, the exceptional point carries fractional topological invariant [16,18,19,24], which unexpectedly induce the stable bulk Fermi-arcs [22,24]. The skin effect in open boundary systems, is associated with the bulk topology in point gaps [15,16,17,18,21,23]. Besides, recent discoveries of lines, rings and surfaces of exceptional points further enriched the topological classes [25,26,27,28,29]. High order exceptional degeneracies, which are often present as intersections of exceptional lines/surfaces, carry hybrid topological invariant [30].

Lots of efforts have been devoted to classifying exceptional points recently. Topological classification is important, because whenever the energy gaps and Altland-Zirnbauer symmetry for the system is known, the degeneracies within the gap is predictable [14,19,20,31,32]. It is thus a theoretical framework for predicting non-Hermitian topological phases of matter, providing guidance for experimental realizations. The surface of exceptional points is special, because it serves as the horizon between real and imaginary line gaps [20]. Exceptional surface (ES) can be commonly observed in non-Hermitian systems with parity-time inversion symmetry (*PT*) or chiral symmetry [20,25,26,27], and has broad applications in the design of sensing and absorption devices [29,48]. Two or more ESs can

intersect each other, forming stable intersection lines as a higher-order singularities, which are protected by the symmetry of the system [34,35]. However, upon various important physical phenomena and applications, the ESs and their intersections have never been topologically classified.

In this work, we consider a generic non-Hermitian *PT* symmetric systems with an additional pseudo-Hermitian symmetry, and such systems present complete intersection lines (CIL) of ESs. By analyzing equivalent relations of eigenstates in gaps and on ESs, we discovered that the quotient space of the momentum space is homotopy equivalent to "figure eight". The topology of the structure is thus represented by the fundamental group, which is a free non-Abelian group given by the product of two generators. The topological charges in the group can be associated with the polarization conversion process of the eigenstates. Hybrid topological invariant for intersection singularities can also be elucidated with the group structure. Besides, the conservation of topological charges systematically illustrate the variation of ESs and CILs against the deformations to the Hamiltonian.

The considered Hamiltonian is a two-level system, which is *PT* symmetric and also preserves an additional η-pseudo-Hermitian symmetry [36,37]

$$[H, PT] = 0, \qquad \eta H \eta^{-1} = H^{\dagger} \tag{1}$$

The *PT* operator can be regarded as a complex conjugate, and thus the Hamiltonian can always be gauged to be real. The pseudo-Hermitian operator here takes the Riemannian metric [38,39,13] form $\eta = \mathrm{diag}(-1,1)$. It is notable that η is not unique, in case that the Hamiltonian perform unitary transformations, η transforms simultaneously (see [40] for details). The symmetries impose the Hamiltonian to be expanded

$$H(\mathbf{k}) = f_2(\mathbf{k}) i\sigma_2 + f_3(\mathbf{k})\sigma_3 \tag{2}$$

where $f_{2,3}$ are real functions of **k**-space, and $\sigma_{2,3}$ are Pauli matrices. The identity can be ignored because it has no impact on the gapless structure. Such Hamiltonians correspond to systems with non-reciprocal hopping [41,43] of orbitals. Solving the eigenenergies of the Hamiltonian, one discovers that the band structure shows ESs at $f_2 = \pm f_3$, and these surfaces intersect completely (CIL) at $f_2 = f_3 = 0$. The CIL is stable against deformations to the Hamiltonian, which is a higher order singularity compared with the ESs.

To derive the topological structure stabilizing the CIL, we firstly need to consider the gapless structure of the parameter space. Here the classification is based on the quotient space, and more mathematical techniques on constructing quotient space is shown in Section 2 of [40]. The **k**-space is partitioned into several regions by the ESs. As shown in Fig. 1a, the red and blue lines (ES_1 and ES_2) denote ESs satisfying $f_2 = \pm f_3$, respectively. In regions I and III (satisfying $|f_2| < |f_3|$), the eigenenergies are real, which are *PT*-exact phases. Conversely, regions II and IV (satisfying $|f_2| > |f_3|$) are *PT*-broken phases, having a pair of complex conjugate eigenenergies. It is observed that the antipodal points on ESs have the same eigenstate, which is an equivalent relation, and the two points can be identified. A quotient space can thus be constructed by gluing antipodal points on ESs [45], forming two circular cones with their vortices coincide and ESs being generatrices (see Fig. 1b). A plane perpendicular to the cone axis intersects the cone at a circle (i.e. S^1). The antipodal points on the circle lies in opposite regions [i.e. region I (II) to region III (IV)] in the parameter space (changing the signs of f_2 and f_3, see Fig. 1a). Observing the Hamiltonian (Eq. 2), we discover that by changing the signs of f_2 and f_3, the same eigenstates can be obtained, with only the corresponding eigenenergies exchanged (see [40] for details). Here in our classification, such pair of points are identified as an equivalent relation, and thus one obtains the quotient $S^1/\mathbf{Z}_2$, which is still a circle. We further notice that any points on a single ES (ES_1 or ES_2) have the same eigenstate. These equivalent relations allow

any point A on ES_1 (also any point B in ES_2) to be dragged towards the common vortex of the double cone, forming a bouquet of two circles (i.e. two circles with the same base point, see the figure eight graph in Fig. 1c). Hence, the quotient space of the parameter space is obtained

$$M = S^1 / \mathbf{Z}_2 \vee S^1 / \mathbf{Z}_2 \cong S^1 \vee S^1 \tag{3}$$

The fundamental group can thus be derived as

$$\pi_1(M, \mathrm{A}) = \mathbf{Z} \otimes \mathbf{Z} \tag{4}$$

which is a free non-Abelian group formed by the product of two generators ($xy \neq yx$). Here the invariants x and y can be characterized by the adiabatic transformation of eigenstates on the yellow and green paths in Fig. 1a. It is notable that these paths are open in the original parameter space, but are closed in the quotient space (i.e. the corresponding yellow and green loops in Fig. 1c).

The topological invariants can be associated with the spin rotation of eigenstates by the adiabatic transformation within the energy gaps. We firstly consider the exact phases (regions I and III), the eigenstates φ_m (m=1,2) are real (without arbitrary phase) and orthogonal under an indefinite inner product $a_{mn} = \langle \varphi_m | \eta \varphi_n \rangle$ (a_{mn}=0 for $m \neq n$, $a_{mn} \neq 0$ for m=n) [36]. However, the inner products for the two eigenstates have opposite signs, revealing the Riemannian geometry [19,38,39] of the adiabatic transformation process (see more details in Section 3 of [40]). Hence, the spin rotation of eigenstates is essentially induced by Lorentz boost. For the yellow path (anti-clockwise) in region I that starts at ES_1 (red) and terminates at ES_2 (blue), the two eigenstates experience bifurcation and coalescence processes, and the evolution processes of eigenenergies and eigenstates as the parameters vary are shown in Fig. 2a1-a2, respectively. Here the sequence of eigenstates is defined by sorting the corresponding eigenenergies (from small to large). It is shown that the two eigenstates accumulate opposite geometric phases, inducing the spin rotation of $\varphi_{1,2}$ with $\mp\pi/2$ (i.e. $\varphi'_{1,2} = \exp(\mp i\pi\sigma_2/2)\varphi_{1,2}$, σ_2 is the second Pauli matrix), respectively. The invariant x can thus be characterized the rotation angle. If we change the sequence of the eigenstates (simultaneously the eigenenergies), the rotation angles for $\varphi_{1,2}$ become $\pm\pi/2$, which corresponds the inverse x^{-1}. It can be found that the topological invariants are sensitive to the sequence of the eigenstates (or eigenenergies), owing to the fact that the considered system is non-Hermitian, and both options of the sequences are possible whenever the path traverses the ESs. In broken phases (regions II and IV), the eigenstates become complex, and are orthogonal under inner product $b_{mn} = \varphi_m^T \eta \varphi_n$ (b_{mn}=0 for $m \neq n$, $b_{mn} \neq 0$ for m=n). The arbitrary phase of φ_m can thus be removed if we normalize the eigenstates with the inner product, and the evolution of eigenenergies and eigenstates on the green path in region II (see Fig. 1a) is shown in Fig. 2b1-b3. We find that the two components of the eigenstates keep negative conjugate in the adiabatic transformation. This process converts the polarizations of eigenstates $\varphi_{1,2}$ to the perpendicular direction, and simultaneously the two real vectors are brought to purely imaginary ones. The spin rotations of $\varphi_{1,2}$ are thus characterized by an angle of $\mp\pi/2$ ($\varphi'_{1,2} = \exp(\mp i\pi\sigma_3/2)\varphi_{1,2}$, σ_3 is the third Pauli matrix), representing the invariant y in the group. It is shown that the invariant y is essentially different from x, as the spin rotations are along different axis (characterized by $\sigma_{2,3}$ respectively). By changing the sequence of eigenstates, one also obtains the inverse invariant y^{-1}, similar to x. The evolutions of eigenstates on the paths in regions III and IV are the same as those in regions I and II, and only the corresponding eigenenergies exchanges.

Having understood the invariants x and y, one can easily discover that paths (or loops) carrying non-trivial topology have to traverse ESs (or with terminals on ESs). A loop l without touching any ESs

is confined within a specific region (see Fig. 3a), and is always trivial because it cannot enclose any singularity (or several pairs of annihilable singularities). By moving the loop across the ES, the loop l becomes a composite of two paths l_1 and l_2, as shown in Fig. 2b. Such paths with two terminals on the same ES are also trivial, and one can easily check that eigenstates do not accumulate geometric phase on these paths. Stretching the loop to cross the other ES (see Fig. 3c), the loop l is thus a composite of paths l_1-l_4. Path l_2 and l_4 are in opposite directions (see the arrows in Fig. 3c) and unified sequence of eigenstates, and can be assigned y^{-1} and y, leading to a trivial product $y^{-1}y=1$ (l_1 and l_3 are trivial). However, if one changes the sequence of eigenstates on one of the path (l_2 or l_4), the product becomes non-trivial y^2 or y^{-2}, which cannot deform to the original loop l. The non-commutativity of x and y can be understood as follows. The invariant xy characterizes the path that starts and ends at ES1 (red), and traverses ES2 (blue) in the middle (see Fig. 3d). However, the path for yx is just the opposite, which starts and ends at ES2 and traverses ES1 (see Fig. 3e). Note that here we have fixed the sequence of eigenstates. The analysis above allows us to discuss the hybrid topological invariant of a loop circulating the NIL. Such a loop will inevitably traverse the ESs four times, which corresponds to a composite of four loops in the quotient space, and its topology will have $2^4=16$ options by considering different combinations of x, y and their inverses (see Table. S1 in [40]). Since x and y do not commute, these topological invariants will leads to different variation processes of eigenenergies and eigenstates. The topology on closed loops traversing ESs is well defined only when the sequence of eigenstates is specified. To overcome the ambiguity whenever a path traverses ESs, in the rest of the letter we will use the convention that the eigenstates are sorted by the corresponding eigenenergies (from small to large) in exact phases, and by the sign of imaginary parts of complex eigenenergies (from negative to positive) in broken phases. The invariant on the closed loop circulating the CIL is $xyx^{-1}y^{-1}$ (anti-clockwise loop) or $yxy^{-1}x^{-1}$ (clockwise loop) under this convention. It is notable that the product is not trivial, because x and y do not commute.

With these elementary invariants in the group, we are able to predict the evolution of ESs and CILs as the Hamiltonian deforms. Consider the following example

$$f_2(\mathbf{k}) = k_x k_z,\ f_3(\mathbf{k}) = -k_x^2 + k_y^2 + k_z^2 - d\,. \tag{5}$$

The chain of CILs and ESs in band structure for d=1 are provided in Fig. 4a, where the red and green surfaces denote ES_1 and ES_2 satisfying $f_2 = -f_3$ and $f_2 = f_3$, respectively. We firstly look at the blue loop in Fig. 4a1, which encloses two ESs and their intersections CILs, but does not touch any ESs. Such a loop is trivial according to our previous conclusion, which is not obvious in the figure because these ESs and CILs seemingly prevent the loop from retracting to a point. However, by changing d from positive to negative, the waists of ESs and CIL gradually retract to a point (Fig. 4b1) at the origin, and is finally open up to form a bandgap (Fig. 4c1). The two CILs enclosed by the loop are thus annihilable. The trivial loop enforces the ESs connecting the two CILs to keep smooth as the Hamiltonian deform. This can be explained with the blue elliptic loop on plane k_x=2 (see Fig. 4a1). This loop is segmented by ESs into several paths, as sketched in Fig. 4a2, where the red and green lines denote the ESs intersected on the plane. These two blue loops are equivalent because they enclose the same CILs, and thus the invariants on the path must cancel each other to form a trivial product, meaning that the path l_t is trivial. Hence, the starting and ending points of l_t lie on the same ES without traversing another ES. As one continues to deform the Hamiltonian, the two ESs enclosed will become isolated after the two CILs annihilate (see Fig. 4c1-c2). Now we turn to the orange loop in Fig. 4a1, which was segmented by the ESs into different paths, and the invariant on each path is provided in Fig. 4a3. The invariant on the loop also sets a constraint on the variation of the ESs inside the loop as the Hamiltonian deforms. To preserve the invariant $(yxy^{-1}x^{-1})^2$, there will always be two inannihilable CILs as d varies in the Hamiltonian (Eq. 5). Two CILs touches at a point at d=0 (Fig. 4b1), and the nearby area is partitioned into eight areas (see Fig. 4b3), meaning that it carries a higher invariant $(yxy^{-1}x^{-1})^2$. As one keeps varying

d, the point will be split, and the two CILs becomes isolated, as shown in Fig. 3c1,c3. We thus understand that the invariant $(yxy^{-1}x^{-1})^2$ is a necessary condition for the chain of CILs. Another condition for the presence of the chain of CILs is the mirror symmetries $k_x \to -k_x$ and $k_z \to -k_z$, which will be illustrated later in the tight binding model. The conservation of the invariant also shows that two inannihilable CILs cannot be connected by smooth ESs, as can be observed in Fig. 4a3-c3.

Nonreciprocal tight binding model. The Hamiltonian has a simple form and can be realized with a tight binding model. A scheme of a three-dimensional (3D) fcc lattice model and the corresponding Brillouin zone is shown in Fig. 5a-b, where M and N denote lattice sites. The hopping between M and N (on dark green bonds) is non-reciproal ($M \to N$: t_1, $M \to N$: $-t_1$), and the hoppings on yellow and red bonds (between the same lattice sites but on different directions, i.e. $M(N) \to M(N)$: $\vec{r}_{M(N)} \to \vec{r}_{M(N)} + \vec{a} + \vec{b}$ and $\vec{r}_{M(N)} \to \vec{r}_{M(N)} + \vec{a} - \vec{b}$) are characterized by t_2 and $-t_2$, respectively. The corresponding model is given by

$$\begin{aligned} H = & \sum_{\substack{\vec{r}_M \in \vec{G}_M \\ \vec{\alpha}=\vec{a},\vec{b},\vec{c}}} t_1 (a^\dagger_{M,\vec{r}_M} a_{N,\vec{r}_\alpha+\vec{\alpha}} + a^\dagger_{M,\vec{r}_\alpha} a_{N,\vec{r}_\alpha-\vec{\alpha}}) - h.c. + E_0 (a^\dagger_{M,\vec{r}_M} a_{M,\vec{r}_M} - a^\dagger_{N,\vec{r}_N} a_{N,\vec{r}_N}) \\ & + \sum_{\substack{\vec{r}_h \in \vec{G}_h \\ h=M,N}} t_2 (a^\dagger_{h,\vec{r}_h} a_{h,\vec{r}_h+\vec{a}+\vec{b}} + a^\dagger_{h,\vec{r}_h} a_{h,\vec{r}_h-\vec{a}-\vec{b}} - a^\dagger_{h,\vec{r}_h} a_{h,\vec{r}_h+\vec{a}-\vec{b}} - a^\dagger_{h,\vec{r}_h} a_{h,\vec{r}_h-\vec{a}+\vec{b}}) \end{aligned} \tag{6}$$

where E_0 is the onsite energy of M, and N has a negative onsite energy $-E_0$. $\vec{a}$, $\vec{b}$ and $\vec{c}$ are bond vectors between lattice sites M and N, and are perpendicular to each other (see Fig. 5a). The ESs and CILs for E_0=0 are plotted in Fig. 5c, and the range in k_x direction is $[0, 2\pi/d]$, because the chain of CILs is symmetric with respect to <1,0,0> plane (see Fig. 5b). The system has mirror symmetries $k_x+\pi/d \to -k_x+\pi/d$ and $k_y \to -k_y$ for E_0=0, and also the invariant $(yxy^{-1}x^{-1})^2$ on the orange loop ensure the presence of intersection points of CILs (black arrows). The nonzero of E_0 can break the mirror symmetries in k_x and k_y directions, which eliminates the intersection points (as shown in Fig. 5d). The number of CILs inside the orange loop and the ESs traversed by the loop remain unchanged so that the invariant in conserved. The blue loop is trivial because it does not touch any ESs, and the degeneracies enclosed are waists of ESs (see Fig. 5c-d), independent of the mirror symmetries. The variation of ESs and CILs in lattice models is consistent with our predictions.

In summary, we topologically classified a generic non-Hermitian two-level system with *PT* symmetry and an additional pseudo-Hermitian symmetry, corresponding to systems with non-reciprocal hoppings [46,47,44]. Such systems present surfaces of exceptional points, which intersect stably in momentum space. We showed that the topology of such gapless structure can be viewed from its quotient space, which is a bouquet of two circles, and its fundamental group is isomorphic to a free non-Abelian group with two generators. Elementary invariants in the group are associated with the spin rotation of eigenstates induced by Lorentz boost in adiabatic transformations. Hybrid topological invariant of intersection singularities is revealed from the group, and also the group structure allows the prediction of the variation of ESs and CILs as the Hamiltonian deforms. Our classification is a global topological description, and does not rely on specific bandgaps. The method of quotient space topology might potentially be extended to classify other intersection singularities, such as high order exceptional points [30,48]. Our work predicts a new topological phase a matter, providing pathways for designing systems

to realize robust topological phases. The classification also provides guidance for the design of relevant devices in sensing and lasing applications using exceptional surfaces and their intersections.

References:

1. Lu L, Fu L, Joannopoulos J D, et al. Weyl points and line nodes in gyroid photonic crystals[J]. Nature photonics, 2013, 7(4): 294-299.

2. Lu L, Joannopoulos J D, Soljačić M. Topological photonics[J]. Nature photonics, 2014, 8(11): 821-829.

3. Abanin D A, Morozov S V, Ponomarenko L A, et al. Giant nonlocality near the Dirac point in graphene[J]. Science, 2011, 332(6027): 328-330.

4. Jiang Z, Zhang Y, Stormer H L, et al. Quantum Hall states near the charge-neutral Dirac point in graphene[J]. Physical review letters, 2007, 99(10): 106802.

5. Lu L, Wang Z, Ye D, et al. Experimental observation of Weyl points[J]. Science, 2015, 349(6248): 622-624.

6. Wu Q S, Soluyanov A A, Bzdušek T. Non-Abelian band topology in noninteracting metals[J]. Science, 2019, 365(6459): 1273-1277.

7. Yang E, Yang B, You O, et al. Observation of non-Abelian nodal links in photonics[J]. Physical Review Letters, 2020, 125(3): 033901.

8. Guo Q, Jiang T, Zhang R Y, et al. Experimental observation of non-Abelian topological charges and edge states[J]. Nature, 2021, 594(7862): 195-200.

9. Soluyanov A A, Gresch D, Wang Z, et al. Type-ii weyl semimetals[J]. Nature, 2015, 527(7579): 495-498.

10. Yang L X, Liu Z K, Sun Y, et al. Weyl semimetal phase in the non-centrosymmetric compound TaAs[J]. Nature physics, 2015, 11(9): 728-732.

11. Yang B, Guo Q, Tremain B, et al. Ideal Weyl points and helicoid surface states in artificial photonic crystal structures[J]. Science, 2018, 359(6379): 1013-1016.

12. Jia H, Zhang R, Gao W, et al. Observation of chiral zero mode in inhomogeneous three-dimensional Weyl metamaterials[J]. Science, 2019, 363(6423): 148-151.

13. Jia H, Zhang R Y, Gao W, et al. Chiral transport of pseudospinors induced by synthetic gravitational field in photonic Weyl metamaterials[J]. Physical Review B, 2021, 104(4): 045132.

14. Gong Z, Ashida Y, Kawabata K, et al. Topological phases of non-Hermitian systems[J]. Physical Review X, 2018, 8(3): 031079.

15. Yao S, Wang Z. Edge states and topological invariants of non-Hermitian systems[J]. Physical review letters, 2018, 121(8): 086803.

16. Shen H, Zhen B, Fu L. Topological band theory for non-Hermitian Hamiltonians[J]. Physical review letters, 2018, 120(14): 146402.

17. Okuma N, Kawabata K, Shiozaki K, et al. Topological origin of non-Hermitian skin effects[J]. Physical review letters, 2020, 124(8): 086801.

18. Leykam D, Bliokh K Y, Huang C, et al. Edge modes, degeneracies, and topological numbers in non-Hermitian systems[J]. Physical review letters, 2017, 118(4): 040401.

19. Bergholtz E J, Budich J C, Kunst F K. Exceptional topology of non-Hermitian systems[J]. Reviews of Modern Physics, 2021, 93(1): 015005.

20. Kawabata K, Shiozaki K, Ueda M, et al. Symmetry and topology in non-Hermitian physics[J]. Physical Review X, 2019, 9(4): 041015.

21. Borgnia D S, Kruchkov A J, Slager R J. Non-Hermitian boundary modes and topology[J]. Physical review letters, 2020, 124(5): 056802.

22. Kawabata K, Bessho T, Sato M. Classification of exceptional points and non-Hermitian topological semimetals[J]. Physical review letters, 2019, 123(6): 066405.

23. Song F, Yao S, Wang Z. Non-Hermitian topological invariants in real space[J]. Physical review letters, 2019, 123(24): 246801.

24. Zhou H, Peng C, Yoon Y, et al. Observation of bulk Fermi arc and polarization half charge from paired exceptional points[J]. Science, 2018, 359(6379): 1009-1012.

25. Zhou H, Lee J Y, Liu S, et al. Exceptional surfaces in PT-symmetric non-Hermitian photonic systems[J]. Optica, 2019, 6(2): 190-193.

26. Okugawa R, Yokoyama T. Topological exceptional surfaces in non-Hermitian systems with parity-time and parity-particle-hole symmetries[J]. Physical Review B, 2019, 99(4): 041202.

27. Zhang X, Ding K, Zhou X, et al. Experimental observation of an exceptional surface in synthetic dimensions with magnon polaritons[J]. Physical review letters, 2019, 123(23): 237202.

28. Yang Z, Hu J. Non-Hermitian Hopf-link exceptional line semimetals[J]. Physical Review B, 2019, 99(8): 081102.

29. Zhong Q, Ren J, Khajavikhan M, et al. Sensing with exceptional surfaces in order to combine sensitivity with robustness[J]. Physical review letters, 2019, 122(15): 153902.

30. Tang W, Jiang X, Ding K, et al. Exceptional nexus with a hybrid topological invariant[J]. Science, 2020, 370(6520): 1077-1080.

31. Wojcik, Charles C., et al. "Homotopy characterization of non-Hermitian Hamiltonians." Physical Review B 101.20 (2020): 205417.

32. Sun X Q, Wojcik C C, Fan S, et al. Alice strings in non-Hermitian systems[J]. Physical Review Research, 2020, 2(2): 023226.

34. Miri M A, Alu A. Exceptional points in optics and photonics[J]. Science, 2019, 363(6422).

35. Özdemir Ş K, Rotter S, Nori F, et al. Parity–time symmetry and exceptional points in photonics[J]. Nature materials, 2019, 18(8): 783-798.

36. Mostafazadeh A. Pseudo-Hermitian representation of quantum mechanics[J]. International Journal of Geometric Methods in Modern Physics, 2010, 7(07): 1191-1306.

37. Mostafazadeh A. Quantum brachistochrone problem and the geometry of the state space in pseudo-Hermitian quantum mechanics[J]. Physical review letters, 2007, 99(13): 130502.

38. Freedman D Z, Van Proeyen A. Supergravity[M]. Cambridge university press, 2012.

39. Frankel T. The geometry of physics: an introduction[M]. Cambridge university press, 2011.

40. supplementary material

41. Helbig T, Hofmann T, Imhof S, et al. Generalized bulk–boundary correspondence in non-Hermitian topolectrical circuits[J]. Nature Physics, 2020, 16(7): 747-750.

42. Wang X, Ptitcyn G, Asadchy V S, et al. Nonreciprocity in bianisotropic systems with uniform time modulation[J]. Physical Review Letters, 2020, 125(26): 266102.

43. Ezawa M. Non-Hermitian non-Abelian topological insulators with PT symmetry[J]. Physical Review Research, 2021, 3(4): 043006.

44. Buddhiraju S, Song A, Papadakis G T, et al. Nonreciprocal metamaterial obeying time-reversal symmetry[J]. Physical Review Letters, 2020, 124(25): 257403.

45. Spanier E H. Algebraic topology[M]. Springer Science & Business Media, 1989.

46. Floess D, Chin J Y, Kawatani A, et al. Tunable and switchable polarization rotation with non-reciprocal plasmonic thin films at designated wavelengths[J]. Light: Science & Applications, 2015, 4(5): e284-e284.

47. Delplace P, Yoshida T, Hatsugai Y. Symmetry-protected multifold exceptional points and their topological characterization[J]. Physical review letters, 2021, 127(18): 186602.

48. Soleymani S, Zhong Q, Mokim M, et al. Chiral Coherent Perfect Absorption on Exceptional Surfaces[J]. arXiv preprint arXiv:2107.06019, 2021.

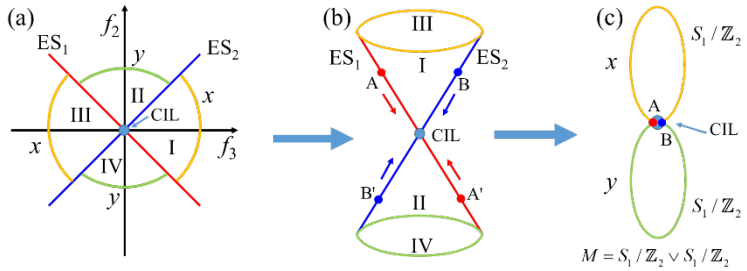

Fig. 1. Construction of quotient space with equivalent relations. (a) The gapless structure of original parameter space, $ES_{1,2}$ characterize exceptional surfaces satisfying relations $f_2=\pm f_3$, respectively. Regions I and III are *PT* exact phases with real line gaps, and Regions II and IV are *PT* broken phases with imaginary line gaps. The ESs intersect (CIL) at $f_2=f_3=0$. (b) Identifying antipodal points on ESs gives a quotient space, which is a double cone with a common vortex. (c) Antipodal points in energy gaps can be identified, and all the points on a single ES can be dragged towards the center, and thus the quotient space being "figure eight" can be constructed.

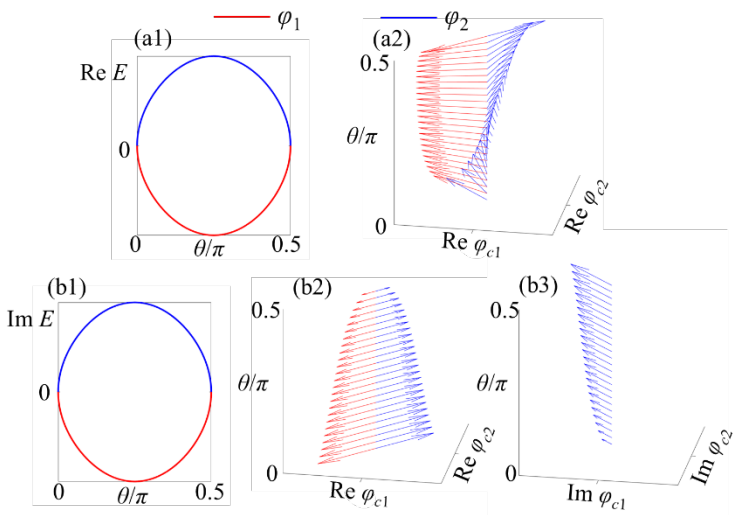

Fig. 2. Characterizing topological invariants x and y with spin rotation of eigenstates. (a1) and (b1) Evolution of eigenenergies on the paths in Regions I and II, respectively (Fig. 1a, anti-clockwise). (a2) and (b1-b2) Spin rotation of eigenstates on the paths induced by Lorentz boost in adiabatic transformations, corresponding to invariants x and y, respectively.

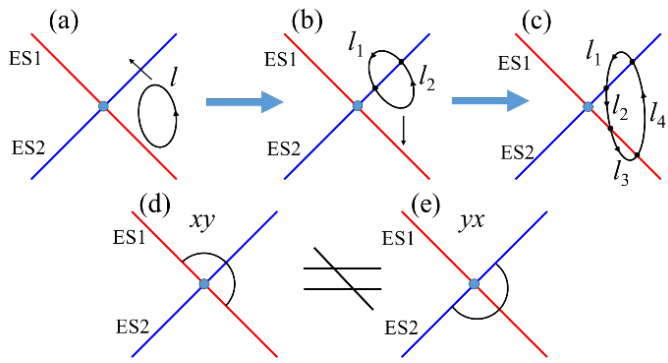

Fig. 3. Trivial loops and non-commutativity of x and y. (a) A loop without touching ESs is confined within a specific region and is trivial. (b) Stretching the loop along the black arrow direction (see (a)), the loop becomes a composite of paths l_1 and l_2. Both of l_1 and l_2 are trivial, and their composite loop is also trivial. (c) Continue stretching the loop along the black arrow direction in (b), the loop crosses ES1 and becomes a composite of l_1-l_4. The invariants on paths l_2 and l_4 can cancel each other if one define the sequence of eigenstates with the corresponding eigenenergies, and the composite loop is still trivial. (d) and (e) paths characterizing invariants xy and yx, respectively. The two path are inequivalent to each other because their starting and ending points are on different ESs, the traversing ESs of the paths are also different.

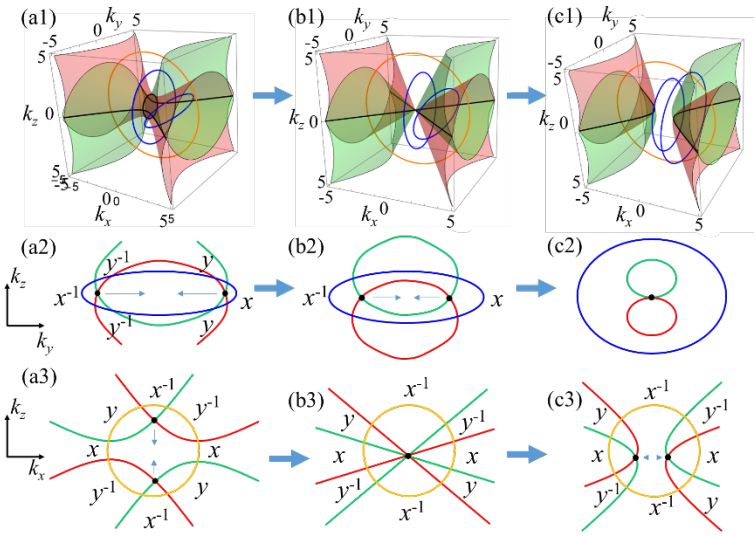

Fig. 4. Evolution of ESs and CILs against deformation of the Hamiltonian. (a1)-(c1) ESs (red and green surfaces) and CILs (black lines) plotted with Eq. 5, corresponding $d>0$, $d=0$ and $d<0$, respectively. The blue loops are trivial. (a2)-(c2) ESs (red and green lines) and CILs (black dots) on the plane that the elliptic loop locates on. The enclosed CILs can annihilate each other. (a3)-(c3) ESs (red and green lines) and CILs (black dots) on the plane that the orange loop locates on. The CILs enclosed cannot annihilate each other.

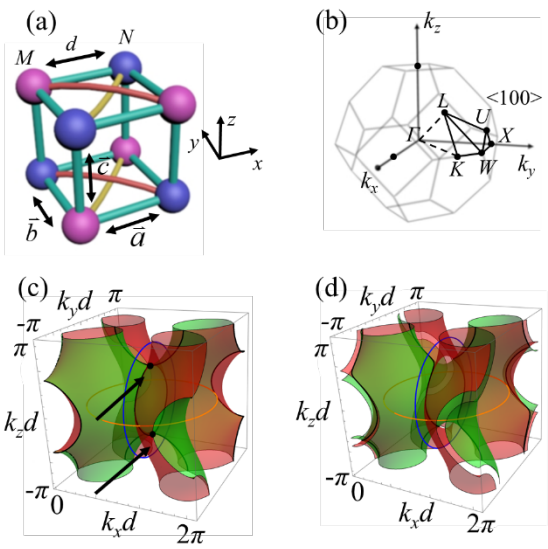

Fig. 5. Proposal of a fcc lattice model with non-reciprocal hoppings. (a) fcc lattice with two sites *M* (blue balls) and *N* (pink balls). The interspace distance between M and N is *d*, and $\vec{a}$, $\vec{b}$ and $\vec{c}$ are bond vectors. The hopping on dark green bonds is nonreciprocal ($M \rightarrow N$: t_1, $M \rightarrow N$: $-t_1$). The hopping on the same lattice sites in different directions (in $\vec{a}+\vec{b}$ and $\vec{a}-\vec{b}$) have opposite signs (hopping on yellow bonds: t_2, hopping on red bonds $-t_2$). (b) First Brillouin zone of the fcc lattice. (c)-(d) ESs (red and green surfaces) and CILs (black lines) for $E_0=0$ and $E_0 \neq 0$ in Eq. 6. (c) has a chain of CILs, which is symmetric with respect to <100> plane. The intersecting points on the chain are labelled with black arrows.